Special Issue

Eletrônica de Potência
Open Journal of Power Electronics

Received July 31, 2024; accepted December 20, 2024; Date of publication February 06, 2025.
The review of this paper was arranged by Associate Editor Renata O. de Sousa and Editor-in-Chief Heverton A. Pereira.

Digital Object Identifier http://doi.org/10.18618/REP.e202516

Integrating Multiple Control Actions in Advanced Microgrids: an Analogy to Well-Established Inverter Control

João M. S. Callegari[1,*], Lucas S. Araujo[1], Dener A. de L. Brandão[1], Braz J. Cardoso Filho[1], Danilo I. Brandão[1]

[1]Universidade Federal de Minas Gerais, Graduate Program in Electrical Engineering, Belo Horizonte, MG, Brazil.

e-mail: jmscallegari@ufmg.br*; savoilucas@ufmg.br; dener.brandao@ieee.org; braz.cardoso@ieee.org; dibrandao@ufmg.br
*Corresponding author

ABSTRACT This paper proposes multiple control actions applied to centralized advanced microgrids (MGs). The well-established control actions feedback (*FB*), feedforward (*FF*), and disturbance decoupling (D) commonly used in current control of distributed energy resources (DERs) are herein extended to advanced MGs. Analytical expressions are derived to show the effect of each control action on the well-established DER current control and then on advanced MG control. Comprehensive comparisons between the feedback and all control action strategies are performed for both DER and MG controls. Simulation and experimental results show a dynamic response improvement in load disturbance rejection when all control actions are considered, as well as a reduction in steady-state error for the grid power flow control. By employing low-bandwidth communication between DERs and central controller, no hardware retrofit is required in comparison to what is needed in other state-of-the-art centralized MG controls.

KEYWORDS Centralized advanced microgrid, disturbance decoupling control, feedback control, feedforward control.

I. INTRODUCTION

Advanced microgrid (MG) models offer a promising solution to address power quality issues arising from the widespread integration of distributed energy resources (DERs) [1]. These advanced MGs organize loads and DERs within clearly defined electrical boundaries and provide several key features [2]: (i) power dispatchability at the point of common coupling (PCC), allowing the MG to function as a single controllable entity from the perspective of the upstream grid; (ii) efficient power sharing among DERs; and (iii) the ability to operate in both grid-connected and islanded modes.

Many control strategies are found in the literature to properly manage advanced MG models. The aforementioned features can be satisfactorily achieved by adopting centralized MG architectures equipped with low-bandwidth communication infrastructure [3]. In centralized architectures, a central controller (CC) steers all participating DERs to achieve efficient MG management and provide ancillary services such as PCC power flow control [4], voltage support and harmonic compensation [5], current unbalance mitigation [6], and improved frequency/voltage deviation [7].

Although several strategies that align with the definition of advanced MGs are outlined in the literature, enhancing the response dynamics of these strategies can be readily achieved by also incorporating control actions in its formulation. This practice is widely implemented in the well-established current control of DERs, where feedback (*FB*), feedforward (*FF*), and disturbance decoupling (D) actions are incorporated to enhance the dynamic response of the inverter without requiring hardware upgrades or complex algorithms. The feedback mechanism in DER control mitigates the error between the injected current and its reference. The feedforward action anticipates changes in the DER current, while disturbance decoupling action mitigates voltage transients at the DER terminals. Several established literature references addressed and evaluated the dynamics of current control from the perspective of control actions [8]–[12], a focus that has not yet been applied to advanced MG control. For instance, the authors of [8] presented a comparative evaluation of the performance of three state-of-the-art feedback current control techniques (i.e., linear proportional-intergral (PI), deadbeat and hysteresis controllers) for active filter-based DERs. Reference [9] shows feedback current controllers for grid-connected DERs, including PI, proportional-resonant (PR), and deadbeat controllers. The authors also discuss the enhancements achieved by incorporating disturbance decoupling actions during voltage sags. The control actions *FB*, *FF* and D are presented for single-phase uninterruptible power system inverters in [10] and for ac machine drives in [11]. Reference [12] proposes a feedback current control scheme for selective harmonic compensation in shunt active power filters. The authors also incorporate cross-coupling decoupling and line voltage disturbance compensation into their approach.

In the control of advanced MGs, strategies are often not articulated in terms of multiple control actions and typically

rely on a single control mechanism. For instance, the authors of [7] proposed a centralized strategy to reduce frequency and voltage deviations within MG nodes through feedback PI controllers devised into a CC. A coordinated feedforward harmonic mitigation and voltage support scheme is proposed in a centralized MG architecture [13], where PCC power dispatchability is not addressed. In [14], it is proposed a centralized MG control embedding feedforward and disturbance decoupling control actions capable of controlling the power flow through the MG PCC. Since the feedback *FB* action is absent in [14], steady-state errors in the PCC power flow control due to non-idealities of communication links and power measurements not properly calibrated may not be compensated. The authors of [15] proposed a MG power dispatch control based on the feedback action with a PI controller and evaluated the effect of communication delays on the MG operation. Other control actions or controller tuning procedures have not been incorporated in [15]. Araujo et al. [16] proposed a centralized control strategy for advanced MGs, integrating distributed grid-forming converters and heterogeneous converters. This approach included the formulation and modeling of secondary feedback controllers for voltage and frequency restoration, providing a framework for controller design. Although not yet addressed in this emerging application, the combined feedback, feedforward, and disturbance decoupling control actions can improve the performance of advanced MG control.

In view of the aforementioned, this paper proposes a centralized control applied to advanced MGs, with improved dynamics by employing feedback, feedforward, and disturbance decoupling control actions. To the best of the authors' knowledge, this approach has not yet been adopted for MG control. This paper is an extended version of [17], providing an enhanced state-of-the-art description and presenting experimental results. As contribution, an analogy is drawn between the well-established current control applied to electronic converters [9], [10], [18] and the centralized MG control, highlighting that well-applied simple concepts can lead to significant improvements in the dynamic control of MGs without introducing unnecessary complexity. The analogy with DER control strengthens the appeal of the proposed strategy by translating the complex MG context into a more well-known framework. Dynamic response improvements of load disturbance rejection and reference tracking are demonstrated by means of simulation and experimental results on a single-phase residential advanced MG. Controller tuning methodology is also addressed, which can be extended to any advanced centralized MG model.

This paper is outlined as follows: Section II presents the description of the DER conventional current control regarding the feedback, feedforward, and disturbance decoupling control actions. Section III shows the control actions applied to the centralized advanced MG control. Sections IV and V show comparative simulation and experimental results, respectively. Conclusions are stated in Section VI.

II. CONTROL ACTIONS APPLIED TO CONVENTIONAL DER CURRENT CONTROL

Figure 1(a) shows the single-phase current-controlled inverter-based DER analyzed herein. It is an H-bridge in-

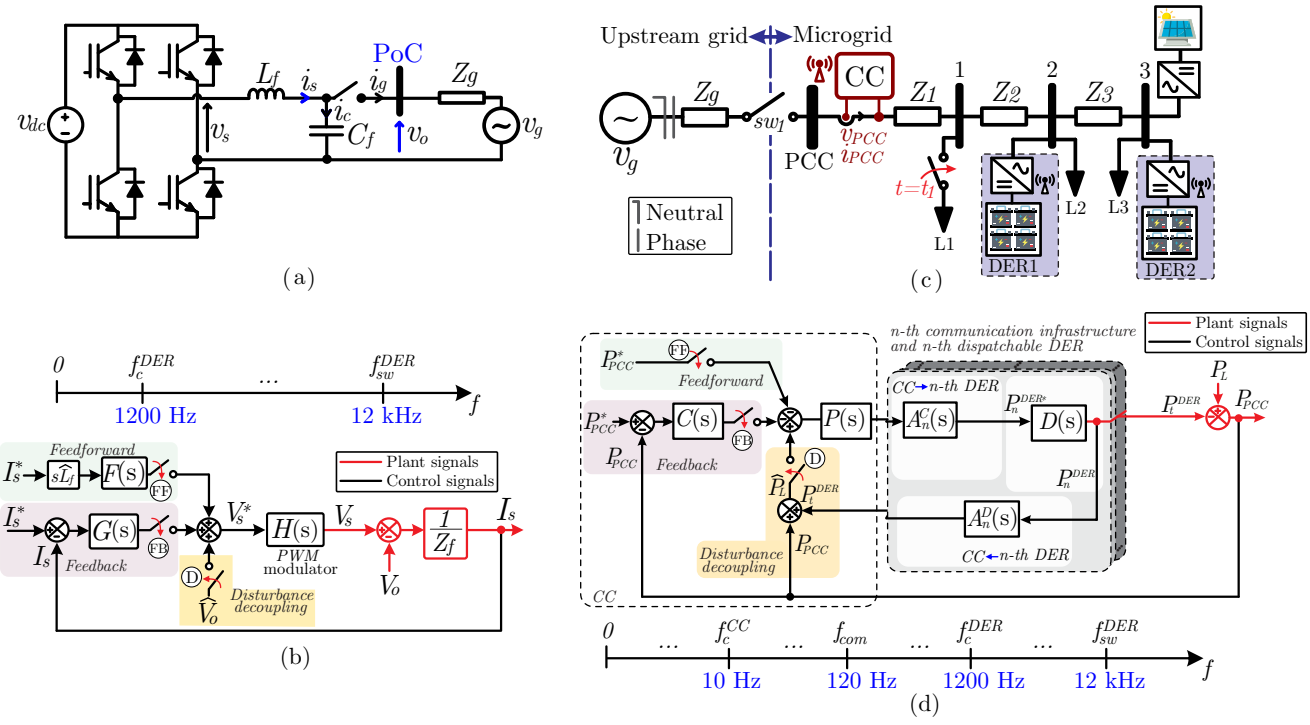

FIGURE 1. (a) Hardware and (b) control diagrams of the DER. (c) Single-phase MG topology. (d) Proposed centralized MG control diagram.

verter with LC filter to suppress the harmonic components produced by the switching [19]. The dc stage is modeled as an ideal dc voltage source (i.e., v_{dc}) without loss of generality. Lowercase and uppercase variables are time-varying and frequency-domain signals, respectively - see Figures 1(a) and (b). v_o is the DER point of connection (PoC) voltage and i_s is the DER controlled current. Since the converter switching frequency $f_{sw} = 12$ kHz is much higher than the DER current controller bandwidth f_c^{DER} = 1.2 kHz - see Figure 1(b), the circuit of Figure 1(a) can be simplified by its average model [20].

Figure 1(b) shows the DER closed-loop control block diagram in Laplace domain, in which: (i) H(s) models the pulse-width modulation (PWM) unit (i.e., including modulator and analog-to-digital conversion delays); (ii) $Z_f = s \cdot L_f + R_f$ is the DER output filter impedance; (iii) G(s) is the proportional-resonant (PR) current controller; (iv) $\widehat{L_f}$ is an estimate of the DER filter inductor (i.e., DER hardware design information); and (v) F(s) is a low-pass filter (LPF) to attenuate the derivative term $s\widehat{L_f}$. Control and plant signals are black and red colored, respectively. In such a block diagram, I_s is the controlled output variable, while I_s^* and V_o are the model inputs (i.e., reference and disturbance). By enabling switches (FB), (FF), and (D) in Figure 1(b), feedback, feedforward, and disturbance decoupling actions are performed, respectively. The DER closed-loop control is given by (1), which lists all the aforementioned input and output terms:

$$I_s = I_s^* \frac{\overbrace{G \cdot H}^{\text{FB}} + \overbrace{s\widehat{L_f} \cdot H}^{\text{FF}}}{Z_f + \underbrace{G \cdot H}_{\text{FB}}} + V_o \frac{\overbrace{H}^{\text{D}} - 1}{Z_f + \underbrace{G \cdot H}_{\text{FB}}} \quad , \qquad (1)$$

where the terms inserted by the feedback, feedforward, and disturbance decoupling actions are highlighted by (FB), (FF), and (D), respectively. The feedback control is responsible for mitigating the error between I_s and I_s^*, where G(s) must be properly tuned to achieve this task. Feedforward and disturbance decoupling actions provide anticipatory action to I_s changes and decouple the PoC voltage transients, respectively. Feedforward action is performed by $I_s^* \cdot s\hat{L}_f$. A wide bandwidth LPF F(s) is employed to reduce the effect of the derivative function s, whose cutoff frequency is ω_f. The PoC voltage, $\widehat{V}_o$, that disturbs the DER current control is also added to the DER controller output to decouple the disturbance in Figure 1(b).

By enabling only the feedback control action, only switch (FB) is closed in Figure 1(b). The terms in (1) highlighted by (FF) and (D) are null since these actions are absent. The current controller tuning is designed one decade apart from the DER switching frequency and lower than the LC filter resonance frequency, following the guidelines of [21]. Equation (1) is complete when all control actions are employed. The feedforward control action affects I_s/I_s^* in (1), while the disturbance decoupling action affects I_s/V_o. The terms in (1) highlighted by (D) show that V_o is compensated if H(s) = 1, which shows disturbance decoupling up to the bandwidth limit of H(s).

III. CONTROL ACTIONS APPLIED TO CENTRALIZED ADVANCED MG CONTROL

Figure 1(c) shows the diagram of the single-phase low-voltage MG topology, with constant-power-modeled loads (i.e., L1, L2, and L3), a non-dispatchable photovoltaic (PV)-based DER, and two single-phase multi-task dispatchable DERs. Herein, dispatchable DERs are configured to operate in current-controlled mode (CCM). However, DERs can operate in either CCM or voltage-controlled mode (VCM), as long as they can track power references transmitted from the CC. For VCM, cascaded power, voltage, and current control loops are required [22]. However, this mode is beyond the scope of this paper. The CC is installed at the MG PCC, where current (i_{PCC}) and voltage (v_{PCC}) measurements are performed. Figure 1(d) shows the evaluated active power loop control diagram. Since active and reactive powers are orthogonal to each other (i.e., decoupled), analyses can be conducted individually for each power term without loss of generality. The communication link enables the CC to gather information from all dispatchable DERs and send control commands to exploit them according to the pursued objectives.

Scaling power coefficients α_P and α_Q are calculated in the CC based on the power conditions of the DER hosting nodes and the MG PCC, following the guidelines in [23]. These coefficients, α_P and α_Q, are then transmitted via a low-bandwidth communication link to set the active P_n^{DER*} and reactive Q_n^{DER*} power references for the DER-embedded control loops. This procedure ensures proportional power sharing based on the capacities of the participating DERs of the MG control. For simplicity, the diagram in Figure 1(d) omits this process, as calculating the power coefficients and applying them to the DER control loops involves no dynamic behavior (i.e., only a static gain normalization). The n-th DER current reference for sinusoidal current synthesis is calculated according to (2), where $P_n^{DER*} = \alpha_P \cdot P_{max,n}^{DER}$ and $Q_n^{DER*} = \alpha_Q \cdot Q_{max,n}^{DER}$. V_{PoC}^{RMS} is the RMS voltage measured at the DER PoC; $\cos(\theta)$ and $\sin(\theta)$ are unity in-phase and quadrature signals synchronized at the DER PoC voltage given by a phase-locked loop algorithm [24]. Notably, the maximum available active power of the DER, $P_{max,n}^{DER}$, depends on the state of charge of the energy storage system integrated with the n-th DER. The maximum reactive power of the DER, $Q_{max,n}^{DER}$, is determined by the remaining power capacity up to the DER rated power rating [23].

$$i_s^* = \frac{\sqrt{2} \cdot P_n^{DER*} \cdot \cos(\theta)}{V_{PoC}^{RMS}} + \frac{\sqrt{2} \cdot Q_n^{DER*} \cdot \sin(\theta)}{V_{PoC}^{RMS}}, \qquad (2)$$

In Figure 1(d), transfer functions (TFs) A_n^D(s) and A_n^C(s) represent the n-th DER→CC and CC→n-th DER communication infrastructures, respectively. P(s) models the CC delayed response, whose processing frequency is expressed by f^{com}. Power terms are calculated by means of moving average filters (MAFs) M(s), which are modeled by an LPF with bandwidth frequency (ω_c) cascaded with a notch filter tuned to the fundamental line-frequency ω_n [25]. Control and plant signals are black and red colored, respectively. P_t^{DER} quantifies the power injected by all DERs participating in the MG control, specifically those coordinated by the CC. C(s) represents the proportional-integral (PI) controller implemented in the MG CC. D(s) represents the closed-loop DER current control, whose hardware and control diagrams are shown in Figures 1(c) and (d), respectively.

From the comparison of Figures 1(b) and (d), it is noted that the complete MG control is analogous to the well-known autonomous DER control in terms of control actions. Thus, all control techniques previously addressed in the literature can be directly applied to the MG centralized control. In both cases, switches (FB), (FF), (D) enable feedback, feedforward, and disturbance compensation control actions, respectively. Regarding Figure 1(d), the feedback control is responsible for mitigating the error between PCC active power, P_{PCC}, and PCC active power reference, P^*_{PCC}, where the controller C(s) must be properly designed to achieve this task. Similarly, in Figure 1(b), the proportional-resonant (PR) controller, G(s), is responsible for mitigating the error between the sinusoidal reference, I_s^*, and the measured DER current, I_s.

Feedforward action provides action in advance of a change in the P_{PCC}, by adding the feedforward signal to the C(s) output. This control action is analogous to the one performed in Figure 1(b), by means of $I_s^* \cdot s\hat{L}_f$ term. Finally, the disturbance decoupling action, $\hat{P}_L$, decouples the MG load transients (i.e., P_L). The estimation of $\hat{P}_L$ is developed according to [14], in which $\hat{P}_L$ is computed within one CC control cycle. The procedure to estimate $\hat{P}_L$ is summarized in the following: (i) the n-th DER unit transmits to the CC the individual active power provided by the n-th DER unit (P_n^{DER}); (ii) the CC computes the total active power P_t^{DER} provided by the N participating DERs; (iii) monitoring the PCC power flow, the CC estimates the total active ($\widehat{P}_L$) power drained within the MG internal nodes:

$$\widehat{P}_L = \overbrace{\sum_{n=1}^{N} P_n^{DER}}^{P_t^{DER}} + P_{PCC}, \tag{3}$$

where $\widehat{P}_L$ produces the required load disturbance decoupling action due to MG load shedding/connection and/or also power variation of non-dispatchable DERs. Analogously, (4) lists all the aforementioned input and output terms regarding MG centralized control:

$$P_{PCC} = P^*_{PCC} \frac{A_n^C \cdot D \cdot P \cdot (\overbrace{C}^{\text{FB}} + \overbrace{1}^{\text{FF}})}{1 + A_n^C \cdot D \cdot P \cdot (\underbrace{1 - A_n^D}_{\text{D}} + \underbrace{C}_{\text{FB}})} + P_L \frac{\overbrace{1 - A_n^C \cdot A_n^D \cdot D \cdot P}^{\text{D}}}{1 + A_n^C \cdot D \cdot P \cdot (\underbrace{1 - A_n^D}_{\text{D}} + \underbrace{C}_{\text{FB}})}. \tag{4}$$

A suitable control strategy must effectively track P^*_{PCC} and reject P_L disturbance. As noted, the feedback action affects both the P_{PCC}/P^*_{PCC} and P_{PCC}/P_L TFs. The feedforward control action affects P_{PCC}/P^*_{PCC}, and the disturbance decoupling action affects the numerator of P_{PCC}/P_L. The terms inserted in (4) by the control actions are highlighted by (FB), (FF) and (D). Equation (4) is complete if the three control actions are enabled.

The tuning of the centralized controller and the processing time of CC are designed with different dynamics for proper MG operation: (i) DER switching frequency is 12 kHz - vide f_{sw}^{DER} in Figures 3(b) and (d); (ii) current controller is tuned with cutoff frequency f_c^{DER}, one decade below the switching frequency (i.e., 1.2 kHz) - lower than the LC filter resonant frequency (i.e., 2 kHz); (iii) the processing time and data exchange between DERs and CC is set to f_{com} =120 Hz, one decade below the DER current control bandwidth; and (iv) the centralized PI controller, implemented in CC, is tuned to cutoff-frequency of f_c^{CC} =10 Hz, 90° phase margin, according to the method described in [21]. The non-compensated open-loop TF, G_{OL}(s), of the secondary control from Figure 1(d) is:

$$G_{OL}(\text{s}) = C(\text{s}) \cdot A_n^C(\text{s}) \cdot D(\text{s}) \cdot P(\text{s}), \tag{5}$$

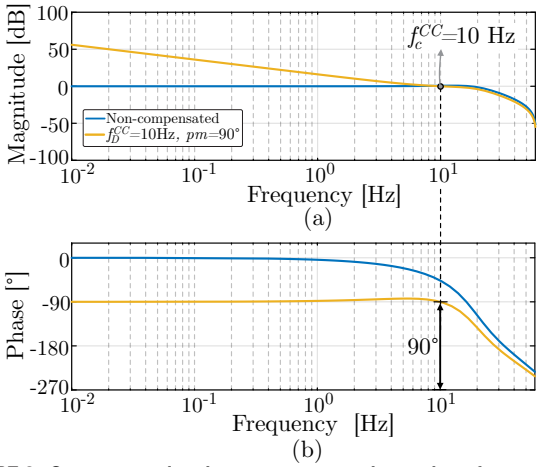

FIGURE 2. Compensated and non-compensated open-loop frequency response of the MG centralized control with feedback action: (a) magnitude, and (b) phase.

where D(s) is the DER closed-loop TF, I_s(s)/I_s^*(s), defined in (1), cascaded with a MAF - see (6). DER is power open-loop controlled. P(s) is defined in (7) by means of a zero-order holder TF tuned at frequency f_{com} or period T_{com}, and adjusted using the Padé approximant method. A_n^C is defined in (8), where T_n^C is transmission time from CC to n-th DER. The centralized PI controller C(s), defined in (9), can be tuned from (5) according to the previous assumptions (i.e., f_c^{CC} =10 Hz and phase margin of 90°). The magnitude and phase response of Figure 2 shows that f_c^{CC} and pm are reached.

$$D(\mathrm{s}) = \overbrace{\frac{G \cdot H + s\widehat{L_f} \cdot H}{Z_f + G \cdot H}}^{I_s/I_s^*} \cdot \overbrace{\left(\frac{\omega_c}{s+\omega_c}\right) \cdot \left(\frac{s^2+\omega_n^2}{s^2 + s \cdot \omega_b + \omega_n^2}\right)}^{M(\mathrm{s})}, \tag{6}$$

$$P(\mathrm{s}) = \frac{1 - e^{-sT_{com}}}{sT_{com}}, \tag{7}$$

$$A_n^C(\mathrm{s}) = e^{-sT_n^C}, \tag{8}$$

$$C(\mathrm{s}) = K_p^{CC} + \frac{K_i^{CC}}{s}. \tag{9}$$

It is worth noting that an anti-windup mechanism is incorporated into the PI controller to prevent deep saturation of the integral term during transients, when the communication link is lost or when the DERs lack sufficient available power to meet the required MG PCC dispatchability. Integrator windup occurs when the integral term in the PI controller accumulates excessively during periods when the controller output is saturated or constrained. This can lead to a significant overshoot and slow recovery when the system returns to normal operation.

IV. SIMULATION RESULTS

Table 1 shows the main parameters of the DERs and single-phase MG. PLECS® platform is adopted in the simulations, with a discrete simulation step of 0.83 μs. The communication link between dispatchable DERs and CC is configured to occur every 1/120 s, with the transmission latency defined in Table 1. The single-phase loads are modeled to drain constant active and reactive power, according to Table 1. Load L1 is connected to MG at t_1 = 1.5 s. The non-dispatchable PV-based DER has the same parameters compared to the dispatchable DERs. The PV-based DER injects a fixed 1000 W during the entire simulated period. The feedback and all control strategies are evaluated considering the same parameters of DER (i.e., well-established current control) and MG (i.e., advanced MG control) to ensure fair comparisons between them.

TABLE 1. Parameters of the DERs and single-phase advanced MG.

DER parameters	Label	Value
DER power rating (simulation/experimental)	S_1^{DER}, S_2^{DER}	6 kVA / 1.5 kVA
Switching/sampling frequency	f_{sw}, f_s	24 kHz
LC filter parameters	L_f, R_f, C_f	2 mH, 150 mΩ, 3.3 μF
dc-link capacitance	C_{dc}	1.17 mF
dc-link voltage (simulation/experimental)	V_{dc}	400 V / 320 V
PoC peak voltage (simulation/experimental)	V_{pk}	$220\sqrt{2}$ V / $127\sqrt{2}$ V
PoC RMS voltage (simulation/experimental)	V_{RMS}^{DER}	220 V / 127 V
Inner loop: P gain	K_p^{inner}	16 Ω
Inner loop: R gain	K_r^{inner}	2000 V^{-1}/s
Estimated filter inductance	$\widehat{L}_f$	2 mH
DER LPF bandwidth	ω_f	$2 \cdot \pi \cdot 10,000$ rad/s
MG parameters	**Label**	**Value**
RMS phase-to-neutral voltage	V_g^{RMS}	127 V, 60 Hz
Fundamental line frequency	ω_n	377 rad/s
Number of participating DERs	N	2
Grid and line impedances	Z_g,Z_1	0.032+j0.012 Ω
	Z_2, Z_4	0.021+j0.002 Ω
	Z_3	0.021+j0.01 Ω
CC controller	K_p^{CC}, K_i^{CC}	0.54, 58.82 s^{-1}
Loads (simulation)	L1	2000 W, 1300 var
	L2	1500 W, 1250 var
	L3	1500 W, 1500 var
Loads (experimental)	L1	1000 W, 0 var
	L2	250 W, 0 var
CC sampling frequency	f_s^{CC}	6 kHz
CC processing frequency (simulation/experimental)	f_{com}	120 Hz / 10 Hz
MAF notch filter bandwidth	ω_b	90 rad/s
MAF LPF bandwidth	ω_c	20 rad/s
Transmission time from CC to n-th DER	T_n^C	0.1 ms
Transmission time from n-th DER to CC	T_n^D	0.1 ms

A. Improved dynamics derived from control actions for DER current control

Figures 3(a)-(e) comparatively show current and voltage waveforms considering the DER control with only the feedback control action and with all control actions (i.e., feedback, feedforward, and disturbance decoupling actions). For fair comparisons, the same controller gains are employed for both cases. Four scenarios are conducted in the simulation results of Figure 3: (i) DER control initialization at 0.5 s, with current reference magnitude set to 10 A; (ii) step from 10 to 20 A of current reference magnitude at 0.8 s; (iii) disturbance of the DER PoC voltage by a 50% residual voltage sag at 0.9 s, maintaining the same DER reference current; (iv) voltage restoration to rated condition (i.e., 127 V) at 1 s.

When all control actions are enabled, the transient of current tracking i_s is visually imperceptible under all performed (i)-(iv) events, as shown in the zoomed views of Figure 3(b)-(e). The absence of transient overcurrents is interesting from the point of view of DER hardware safety, suggesting a stiff control to reference variations and disturbance rejection. On the other hand, a current overshoot of 12.5 A is observed at the DER control initialization when only the feedback action is used - see Figure 3(b). A transient overcurrent of 26.5 A is also noted during the 50% voltage sag, in such a scenario with only feedback action - see Figure 3(d). Although the control results between both cases are similar in the steady-state condition, the transient response of the DER current control deteriorates when using only the feedback

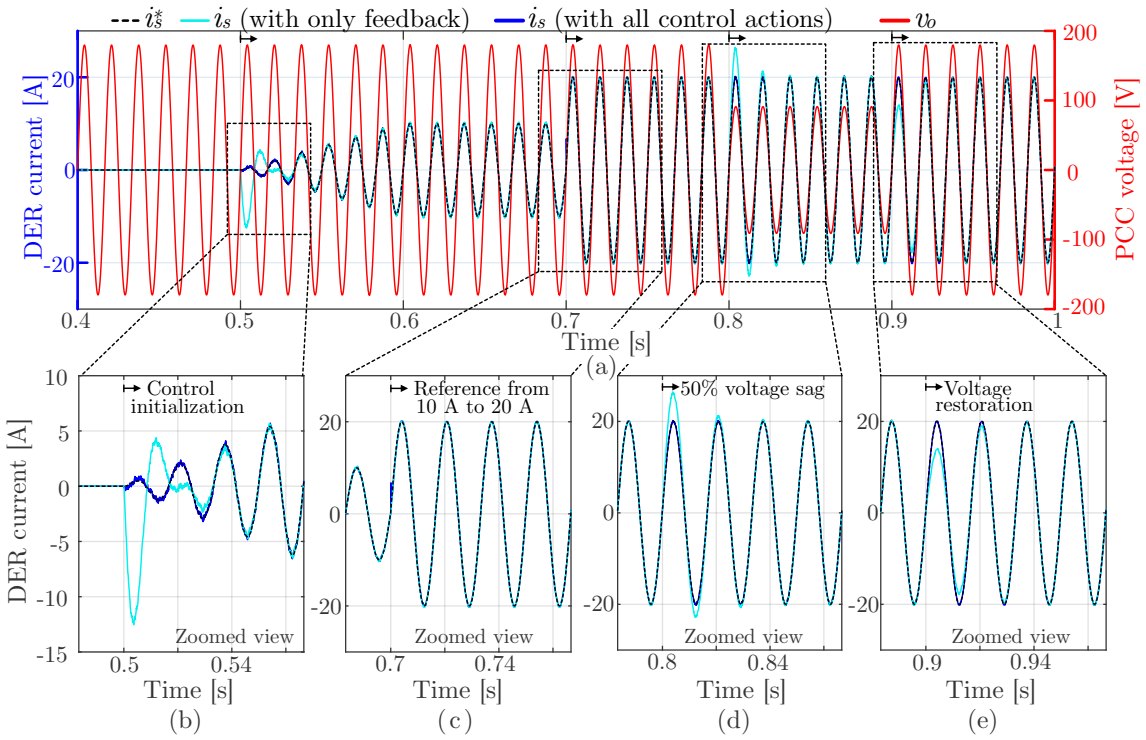

FIGURE 3. (a) Current and voltage waveforms considering the simulated DER control with only the feedback control action and with all control actions. Zoomed views of current waveforms during (b) current control initialization; (c) current reference step from 10 to 20 A; (d)-(e) 50% residual voltage sag.

action. Thus, the feedforward and disturbance compensation actions positively affect the dynamics of the DER current control, without performing a hardware retrofit or additional measurements.

B. Improved dynamics derived from control actions for centralized MG control

1) Reference tracking performance and load disturbance rejection

Two case studies are conducted in the results of Figure 4: centralized MG control with only feedback action; and centralized MG control with all control actions (i.e. feedback, feedforward and disturbance decoupling). Figures 4(a) and (b) show the active and reactive power terms exchanged between the MG and the upstream grid for the entire simulation time. Four scenarios are conducted in the simulation results of Figure 4: (i) MG control initialization at 0.5 s, with null active and reactive power references (i.e., P^*_{PCC} = 0 and Q^*_{PCC} = 0); (ii) load L1 disconnected at t_1=1.5 s, which drains 2 kW and 1.3 kvar; (iii) P^*_{PCC} ramped from 0 to -2000 W at 2 s; and (iv) Q^*_{PCC} ramped from 0 to -5000 W at 2 s. Negative power terms indicate the exportation of active and reactive (i.e., capacitive) power to the upstream grid.

The zoomed views of Figures 4(c) and (d) show the effect of controlled PCC active power during load disturbance L1 and P^*_{PCC} from 0 to -2000 W, respectively. When all control actions are enabled, load disturbance rejection - modeled as P_L and compensated through $\hat{P}_L$ - is improved compared to the MG control with only feedback action.

For instance, when only the feedback action is employed, a deviation of 733 W from the active power reference is observed in the P_{PCC} regulation during the disconnection of L1, as shown by the orange plot in Figure 4(c). In contrast, when all control actions are utilized, the power disturbance is reduced from 733 W to 351 W, leading to approximately a 52% reduction in transient overshoot, as indicated by the blue plot in Figure 4(c). Figure 4(d) shows that the dynamics of reference tracking when changing P^*_{PCC} from 0 to -2000 W is improved with all control actions, due to the feedforward action, compared to the case with only feedback action. This same observation is performed in Figure 4(f), when changing Q^*_{PCC} from 0 to -5000 var. Additionally, the zoomed view of Figure 4(e) shows that the deviation from the zero reactive power reference is 460 var with only the feedback action, compared to 190 var when all control actions are implemented. It is a 61% reduction in transient reactive power deviation at the MG PCC with the proposed strategy, which also shows enhanced disturbance rejection capabilities.

2) Power sharing between DERs and PV generation disturbance rejection

The simulation results of Figure 5 show the centralized MG control with only feedback action and with all control actions, considering PV generation disturbance within MG nodes. Active and reactive power terms exchanged between

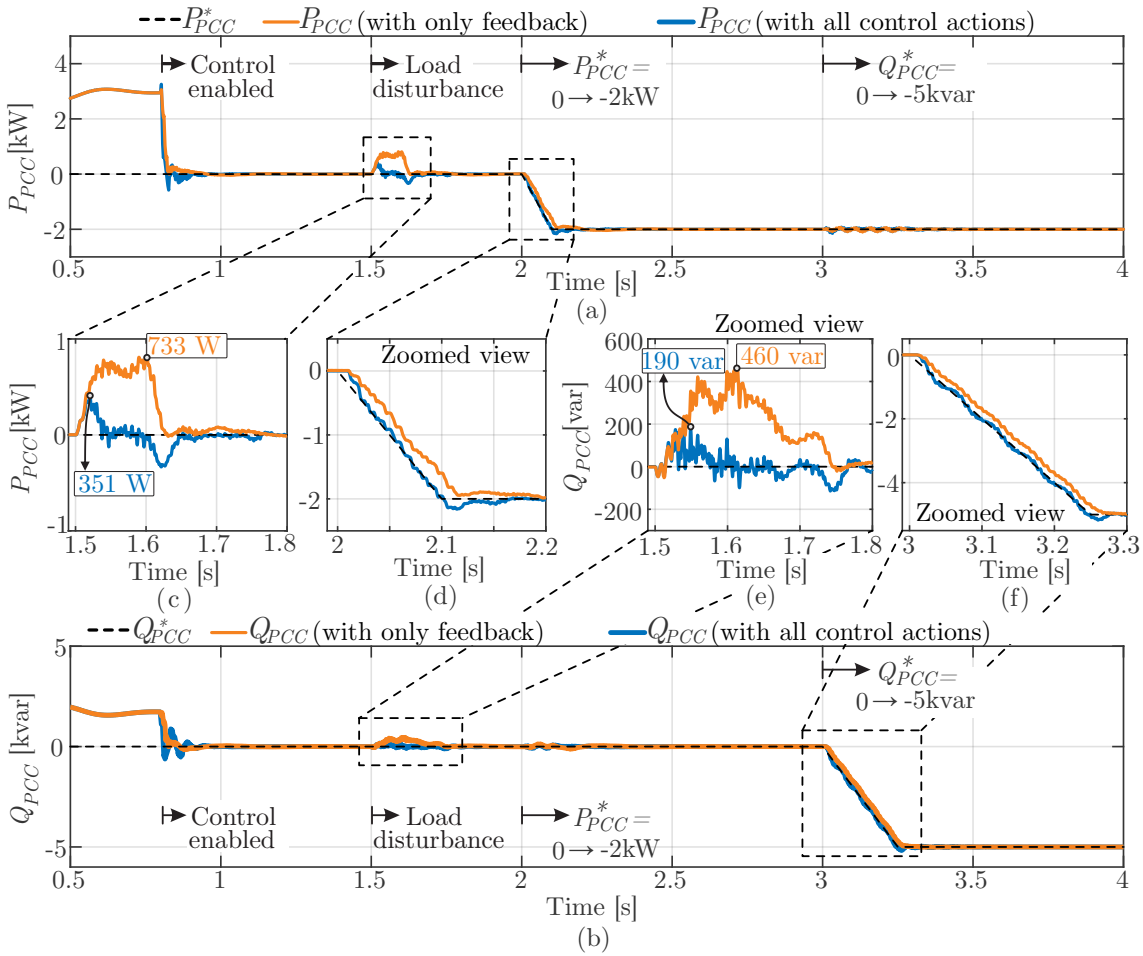

FIGURE 4. (a)-(b) Active and reactive power terms at the PCC, respectively, considering the simulated MG centralized control with feedback and with all control actions. Zoomed views: effect of disturbance on (c) P_{PCC} and (e) Q_{PCC} caused by L1 load disconnection; power reference tracking (d) P^*_{PCC} and (f) Q^*_{PCC} during $P^*_{PCC} = 0 \rightarrow -2000$ W and $Q^*_{PCC} = 0 \rightarrow -5000$ var, respectively.

the MG and the upstream grid for the entire simulation time are shown in Figures 5(a) and (b), respectively. At 0.8 s, P^*_{PCC} and Q^*_{PCC} increase to 0 W and 0 var, with the PV-based DER injecting 1 kW into MG node 3. As noted, PCC reference tracking is improved with all control actions, compared to the case with only the feedback action. At 1.5 s, solar irradiance is emulated from 300 to 700 W/m^2. The PV-based DER increases the active power injection from 1 to 3.5 kW, as shown in Figure 5(a). The zoomed-in view of Figure 5(a) shows the effect of the controlled active power of the PCC during this disturbance for both secondary controls of MG. Generation disturbance rejection - computed through $\hat{P}_L$ - is improved 55% (i.e., from -1565 to -692 W) in terms of the P_{PCC} sinking for all control actions compared to only feedback control. Due to the power couplings caused by the MG line impedances, the PCC reactive power is also disturbed by the PV-based DER active power injection.

The behavior of the coefficients for active, α_P, and reactive, α_Q, power along the simulation scenario considered is reported in Figures 5(c) and (d) for only feedback control. Also, Figures 5(c) and (d) show the active and reactive terms processed by the two dispatchable DERs for MG control with feedback action. Figure 5(e) shows α_P, P_1^{DER} and P_2^{DER}, while Figure 5(e) shows α_Q, Q_1^{DER} and Q_2^{DER} for MG control with all control actions. Since both DERs have the same active power availability and apparent power rating, active and reactive power–sharing capability is observed in Figures 5(c)-(f) for both strategies. When solar irradiance suddenly increases from 300 to 700 W/m^2 (or equivalently, PV-based DER injects from 1 to 3.5 kW), both dispatchable DERs proportionally reduce their active power output to maintain P^*_{PCC} regulation at 0 W.

3) Lack of power capacity of DERs to track CC commands

Simulation results of Figure 6 explore the operating conditions of the centralized MG control with all control actions under limited DER power capability. The following sequence of events is simulated: up to 1.5 seconds, the proposed MG control maintains the $P^*_{PCC} = 0$ W; at 1.5 seconds, the PCC power reference is gradually increased to inject 10 kW to the upstream grid; at 3 seconds, the 3 kW PV-based DER is disconnected; and at 4 seconds, the PCC power reference is gradually reduced back to 0 kW.

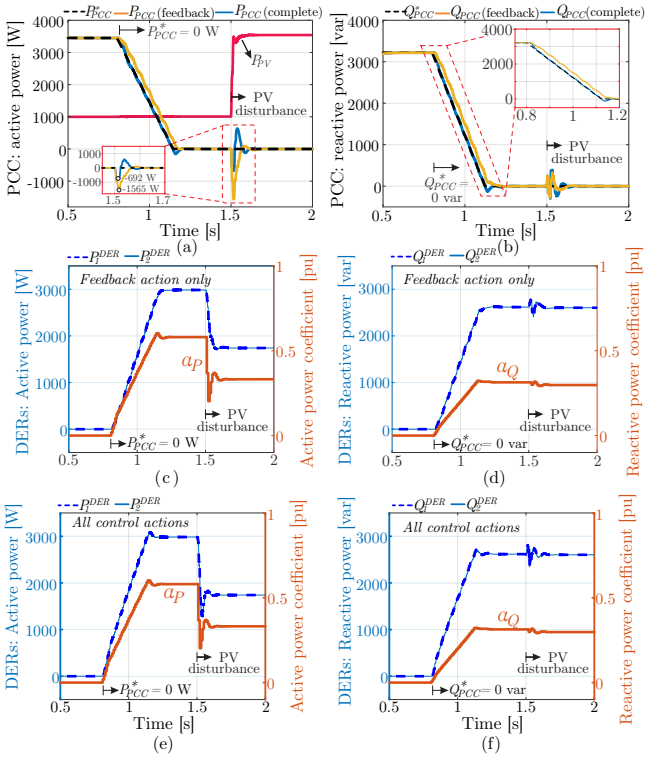

FIGURE 5. (a) Active and (b) reactive power terms at the PCC, considering the simulated MG centralized control with feedback and with all control actions. (c) Active and (d) reactive power-sharing by dispatchable DERs using MG centralized control with feedback action. (e) Active and (f) reactive power-sharing by dispatchable DERs using using MG centralized control with all control actions.

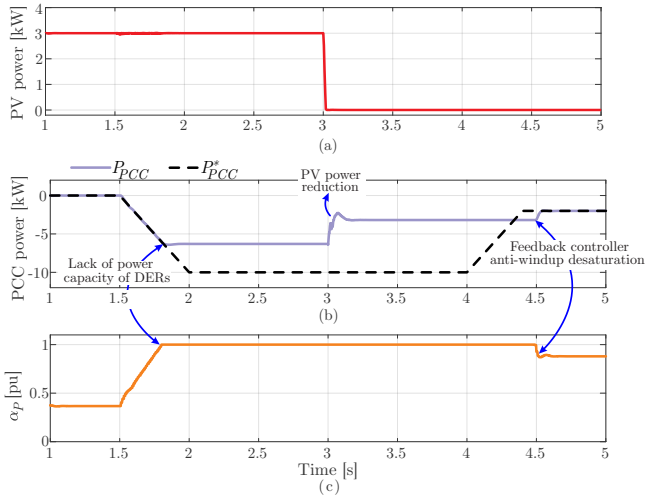

FIGURE 6. (a) Active power generated by the PV-based DER. (b) Active power at the MG PCC and the respective power reference. (c) Power coefficient α_P.

Figure 6(a) shows the active power generated by the PV-based DER. Initially, the DER injects around 3 kW. At 3 seconds, the PV-based DER is disconnected, causing the PV active power to drop abruptly to zero. Figure 6(b) displays the active power at the MG PCC (i.e., P_{PCC}) and the respective power reference (i.e., P^*_{PCC}). Up to 1.5 seconds, the control strategy regulates the PCC power to zero, following the power reference. At 1.5 seconds, the PCC power reference is ramped up to 10 kW (i.e., P^*_{PCC} = -10 kW). However, due to the DER power limitations, the actual PCC power remains below the reference, stabilizing around -6.3 kW.

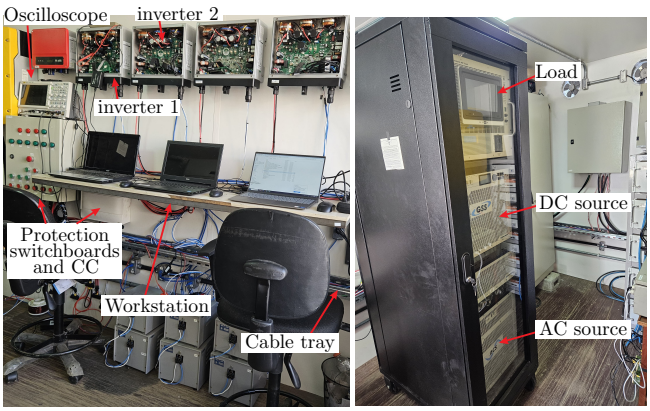

FIGURE 7. Laboratory-scaled single-phase MG prototype. The diagram connection of each piece of equipment is established in Figure 1.

Figure 6(c) shows that the power coefficient α_P reaches its maximum value, which indicates that the DERs inject their maximum available power. The CC feedback controller anti-windup mechanism prevents excessive integrator from accumulating during the period when the controller output is saturated. When the PV is disconnected at 3 seconds, the discrepancy between the PCC active power (i.e., -3.2 kW) and its reference (i.e., -10 kW) further increases, as expected. At 4 seconds, the power reference returns to 0 kW, allowing the actual PCC active power to converge to the reference once more as desaturation of CC feedback controller occurs. When the reference returns to 0 W at 4 seconds, α_P drops below unity, desaturation occurs smoothly, and the PCC power is able to accurately track the reference again.

V. EXPERIMENTAL RESULTS

The laboratory-scale experimental single-phase MG prototype is depicted in Figure 7 and Table 1. Despite the slight differences between the simulation and experimental parameters, the proposed strategy extends readily to both cases with the core findings remaining consistent, as further discussed in this section. Dispatchable DERs are implemented using PHB 1500-NS single-phase off-the-shelf commercial inverters, programmed with the TMS320F28034 fixed-point digital signal processor. The CC is composed of the LAUNCHXL-F28379D, located at the MG PCC. Communication between the CC and dispatchable DERs uses the standard CAN protocol at a communication rate of 125 kbps. The communication link between dispatchable DERs and CC is configured to occur every 1/10 s. MG load variations are emulated by the NHR 9430 18 kW regenerative four-quadrant load, and the upstream grid is simulated by the TC-ACS 30 kVA programmable four-quadrant source. A 4-channel oscilloscope, equipped with A612 and P5200A

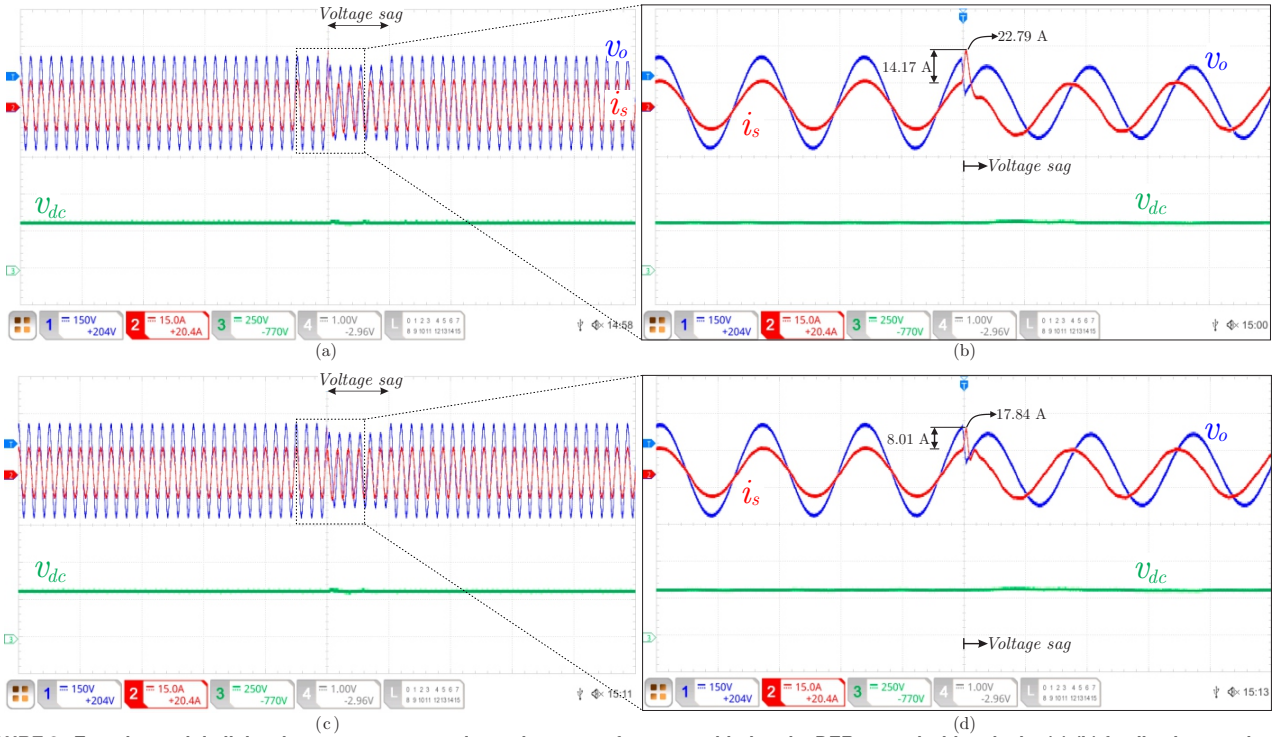

FIGURE 8. Experimental dc-link voltage, ac current, and ac voltage waveforms considering the DER control with only the (a)-(b) feedback control action and (c)-(d) with all control actions.

probes, measures the PCC and DER currents (i.e., i_{pcc}, i_{s1}, and i_{s2}) as well as the PCC voltage (v_{pcc}). More detail can be found in [26], [27]. The datalogger's sampling period is 30 ms. Experimental results are obtained to show the dynamics derived from control actions related to DER current control and centralized MG control.

A. DER current control: improved dynamics derived from control actions

The results in Figure 8 show experimental dynamic response of the DER current control to a voltage sag programmed in the grid simulator. The DER current control is composed of feedback action in Figures 8(a) and (b), and incorporates all control actions in Figures 8(c) and (d). The voltage and current waveforms at the inverter output terminals, along with the DER dc-link voltage are shown in Figure 8. The voltage sag is approximately 20% for a duration of 100 ms, occurring at the peak of the grid voltage in both cases for a fair comparison. Also, the same phase-locked loop synchronization algorithm is used in both cases for a fair comparison.

When only feedback is enabled, a DER current overshoot of 14.17 A occurs at the moment of the voltage sag, reaching an injected current peak of 22.79 A - see zommed view of Figure 8(b). By enabling all control actions, the current overshoot is reduced by 43%, as shown in the zoomed view of Figure 8(d). The overshoot reaches 8.01 A, with a peak of 17.84 A. The disturbance decoupling term plays a crucial role in the results of Figures 8(c) and (d), improving the dynamics of current control during grid voltage variations.

B. Centralized MG control: improved dynamics derived from control actions

Figures 9(a) and (b) show the time-varying signals at the MG PCC and DER terminals for the MG control with only feedback action and with all control actions, respectively. Figure 9 shows seven transitions. In the first (i), MG control is disabled, and the DERs operate in standby mode, processing null power. In the second (ii), MG control is initialized to achieve the self-consumption regime, with both PCC active and reactive power references set to zero. The third scenario (iii) involves connecting load $L1$ to the MG at a rate of 50 A/s. The fourth scenario (iv) shows load $L1$ being disconnected from the MG at the same rate. In the fifth scenario (v), the PCC active power reference P^*_{PCC} is ramped from 0 to 700 W to inject power into the upstream grid. The sixth scenario (vi) involves ramping the PCC reactive power reference Q^*_{PCC} from 0 to 800 var (inductive). Finally, the last scenario (vii) resets both active and reactive power references to zero to achieve grid zero operation.

Figures 9(a.1) and (b.1) show the experimental active and reactive power terms collected at the MG PCC during all events, for the cases with feedback only and with all control actions, respectively. Figures 9(a.2), (a.3), and (a.4) show zoomed views of the transitions (iv)→(v), (v)→(vi), and (vi)→(vii), respectively, extracted from Figure 9(a.1). Similarly, Figures 9(b.2), (b.3), and (b.4) provide zoomed views of these same transitions, sampled from Figure 9(b.1). The PCC signals (i.e., v_{PCC} and i_{PCC}), and the dispatchable DER currents (i.e., $i_{s,1}$ and $i_{s,2}$) for the transition

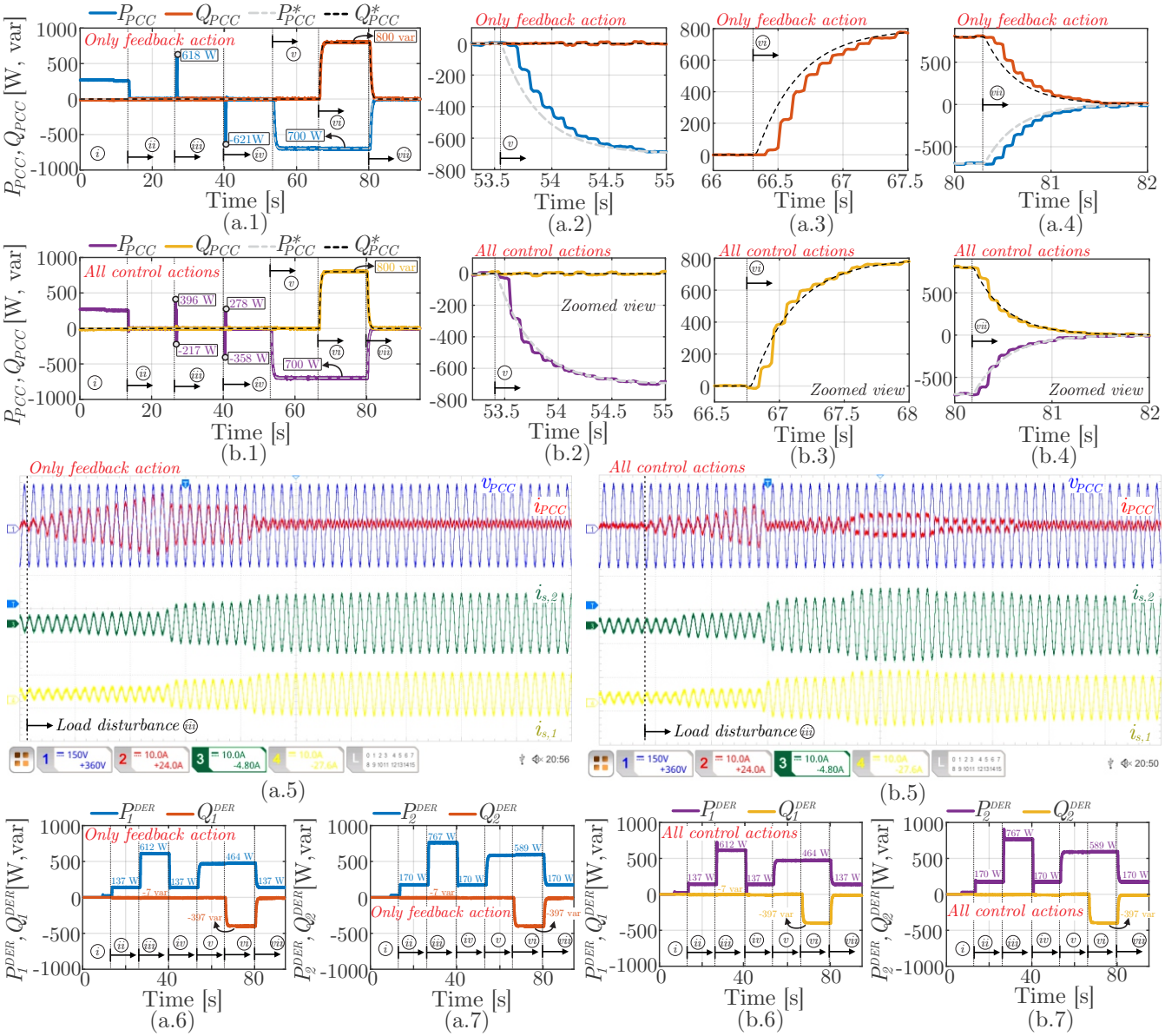

FIGURE 9. Experimental results of MG PCC power terms for the MG control (a) with only feedback action and (b) with all control actions.

$(ii)\rightarrow(iii)$ are shown in Figure 9(a.5) for the strategy with only feedback, and in Figure 9(b.5) for the strategy with all control actions. During the evaluated period, DERs 1 and 2 have active power capacities of 800 W and 1000 W, and reactive power capacities of 800 var each. Due to the inherent proportional power-sharing characteristic of the proposed strategy, DER2 consistently contributes approximately 25% more active power than DER1. This behavior is illustrated in Figures 9(a.6) and (a.7) for the strategy with only feedback, and in Figures 9(b.6) and (b.7) for the strategy with all control actions.

Deviations of 618 W and 621 W are observed in the PCC active power regulation during $L1$ connection and disconnection when only the feedback strategy is adopted - see Figure 9(a.1). In comparison, Figure 9(b.1) shows that the active power deviation from the null reference is significantly reduced to 396 W and 358 W (approximately 36%) during $L1$ connection and disconnection, when disturbance decoupling is incorporated into the MG control with all control actions. This improved load disturbance stiffness is further evident when comparing the results in Figures 9(a.5) and (b.5). The PCC current amplitude deviates less from zero when all control actions are implemented compared to the case in Figure 9(a.5). The Q^*_{PCC} and P^*_{PCC} tracking during $(iv)\rightarrow(v)$, $(v)\rightarrow(vi)$, and $(vi)\rightarrow(vii)$ is also improved when the feedforward action is incorporated into the case with all actions. The tracking delay between the power reference and the power measurement, observed when only the feedback control action is adopted - see Figures 9(a.2), (a.3), and (a.4), is no longer evident when all control actions are implemented

- see Figures 9(b.2), (b.3), and (b.4). The strategy incorporating all control actions shows more accurate reference PCC tracking dynamics, higher stiffness against MG load shedding and MG load connection, compared to the method that relies solely on feedback action.

VI. CONCLUSIONS

This paper proposed a centralized control approach for enhancing the MG response dynamics through feedback, feedforward, and disturbance decoupling control actions. A straightforward relationship between the well-established DER current control and the control of centralized advanced MG was highlighted. The features of feedback-only and all control action strategies were described, and their performances were evaluated through simulation and experimental results in a single-phase MG. The simulation results demonstrated the effectiveness of the all control action strategy in achieving greater disturbance rejection, with a 52% improvement for load rejection and a 55% improvement for generation rejection, compared to the feedback-only strategy. The experimental results showed a 40% improvement in load disturbance rejection and faster PCC power tracking capability with all control actions, achieved with low implementation complexity and without any hardware retrofit to the MG.

In advanced microgrid applications, the most critical aspects for grid-connected MGs are PCC reference tracking and load disturbance rejection. Based on these criteria, the proposed strategy, with its integrated control actions, has proven to be the most effective and suitable for such applications, requiring no hardware retrofit unlike other state-of-the-art centralized MG controls.

AUTHOR'S CONTRIBUTIONS

J. M. S. CALLEGARI: Conceptualization, Data Curation, Formal Analysis, Investigation, Methodology, Software, Validation, Visualization, Writing – Original Draft, Writing – Review & Editing. L. S. ARAUJO: Conceptualization, Formal Analysis, Investigation, Methodology, Software, Supervision, Validation, Visualization, Writing – Review & Editing. D. A. L. BRANDÃO: Conceptualization, Data Curation, Formal Analysis, Investigation, Methodology, Software, Validation, Visualization, Writing – Review & Editing. B. J. CARDOSO FILHO: Conceptualization, Formal Analysis, Funding Acquisition, Methodology, Resources, Supervision, Validation, Visualization, Writing – Review & Editing. D. I. BRANDÃO: Conceptualization, Formal Analysis, Funding Acquisition, Investigation, Methodology, Resources, Supervision, Validation, Visualization, Writing – Review v Editing.

PLAGIARISM POLICY

This article was submitted to the similarity system provided by Crossref and powered by iThenticate – Similarity Check.

REFERENCES

[1] S. Ahmad, M. Shafiullah, C. B. Ahmed, M. Alowaifeer, "A Review of Microgrid Energy Management and Control Strategies", *IEEE Access*, vol. 11, pp. 21729–21757, 2023, doi:10.1109/ACCESS.2023.3248511.

[2] D. Ton, J. Reilly, "Microgrid Controller Initiatives: An Overview of R&D by the U.S. Department of Energy", *IEEE Power Energy Mag*, vol. 15, no. 4, pp. 24–31, 2017, doi:10.1109/MPE.2017.2691238.

[3] A. Muhtadi, D. Pandit, N. Nguyen, J. Mitra, "Distributed Energy Resources Based Microgrid: Review of Architecture, Control, and Reliability", *IEEE Trans Ind Appl*, vol. 57, no. 3, pp. 2223–2235, 2021, doi:10.1109/TIA.2021.3065329.

[4] J. R. Silveira, D. I. Brandao, N. T. Fernandes, W. Uturbey, B. Cardoso, "Multifunctional dispatchable microgrids", *Applied Energy*, vol. 282, p. 116165, 2021, doi:10.1016/j.apenergy.2020.116165.

[5] J. M. S. Callegari, H. A. Pereira, D. I. Brandao, "Voltage Support and Selective Harmonic Current Compensation in Advanced AC Microgrids", *IEEE Transactions on Industry Applications*, vol. 59, no. 4, pp. 4880–4892, 2023, doi:10.1109/TIA.2023.3268644.

[6] D. I. Brandao, T. Caldognetto, F. P. Marafão, M. G. Simões, J. A. Pomilio, P. Tenti, "Centralized Control of Distributed Single-Phase Inverters Arbitrarily Connected to Three-Phase Four-Wire Microgrids", *IEEE Transactions on Smart Grid*, vol. 8, no. 1, pp. 437–446, 2017, doi:10.1109/TSG.2016.2586744.

[7] J. M. Guerrero, J. C. Vasquez, J. Matas, L. G. de Vicuna, M. Castilla, "Hierarchical Control of Droop-Controlled AC and DC Microgrids—A General Approach Toward Standardization", *IEEE Trans Ind Electron*, vol. 58, no. 1, pp. 158–172, 2011, doi:10.1109/TIE.2010.2066534.

[8] S. Buso, L. Malesani, P. Mattavelli, "Comparison of current control techniques for active filter applications", *IEEE Trans Ind Electron*, vol. 45, no. 5, pp. 722–729, 1998, doi:10.1109/41.720328.

[9] A. Timbus, M. Liserre, R. Teodorescu, P. Rodriguez, F. Blaabjerg, "Evaluation of Current Controllers for Distributed Power Generation Systems", *IEEE Trans Power Electron*, vol. 24, no. 3, pp. 654–664, 2009, doi:10.1109/TPEL.2009.2012527.

[10] M. Ryan, W. Brumsickle, R. Lorenz, "Control topology options for single-phase UPS inverters", *IEEE Trans Ind Appl*, vol. 33, no. 2, pp. 493–501, 1997, doi:10.1109/28.568015.

[11] H. Kim, M. W. Degner, J. M. Guerrero, F. Briz, R. D. Lorenz, "Discrete-Time Current Regulator Design for AC Machine Drives", *IEEE Trans Ind Appl*, vol. 46, no. 4, pp. 1425–1435, 2010, doi:10.1109/TIA.2010.2049628.

[12] C. Lascu, L. Asiminoaei, I. Boldea, F. Blaabjerg, "High Performance Current Controller for Selective Harmonic Compensation in Active Power Filters", *IEEE Trans Power Electron*, vol. 22, no. 5, pp. 1826–1835, 2007, doi:10.1109/TPEL.2007.904060.

[13] S. Y. Mousazadeh Mousavi, A. Jalilian, M. Savaghebi, J. M. Guerrero, "Coordinated control of multifunctional inverters for voltage support and harmonic compensation in a grid-connected microgrid", *Electric Power Syst Research*, vol. 155, pp. 254–264, 2018, doi:10.1016/j.epsr.2017.10.016.

[14] D. I. Brandao, L. S. Araujo, A. M. S. Alonso, G. L. dos Reis, E. V. Liberado, F. P. Marafão, "Coordinated Control of Distributed Three- and Single-Phase Inverters Connected to Three-Phase Three-Wire Microgrids", *IEEE J Emerg Sel Topics Power Electron*, vol. 8, no. 4, pp. 3861–3877, 2020, doi:10.1109/JESTPE.2019.2931122.

[15] A. M. dos Santos Alonso, J. B. Ribeiro do Val, "Networked Control of Distributed Energy Systems in Dispatchable Microgrids: System Modeling and Stability Considerations", *in SMART*, pp. 1–9, 2022, doi:10.1109/SMART55236.2022.9990325.

[16] L. S. Araujo, J. M. S. Callegari, B. J. Cardoso Filho, D. I. Brandao, "Heterogeneous microgrids: Centralized control strategy with distributed grid-forming converters", *Int J Electric Power & Energy Syst*, vol. 158, p. 109950, 2024, doi:10.1016/j.ijepes.2024.109950.

[17] J. M. S. Callegari, L. S. Araujo, D. A. De Lisboa Brandão, B. J. Cardoso Filho, D. I. Brandao, "Centralized Strategy Incorporating Multiple Control Actions Applied to Advanced Microgrids", *in 2023 IEEE SPEC/COBEP*, pp. 1–7, 2023, doi:10.1109/SPEC56436.2023.10408015.

[18] T. M. Parreiras, M. H. d. S. Alves, R. R. Bastos, I. A. Pires, B. d. J. Cardoso Filho, "The True Unity Power Factor Converter for Basic Oxygen Furnace Charging Cranes", *IEEE Trans Ind Appl*, vol. 57, no. 5, pp. 5507–5516, 2021, doi:10.1109/TIA.2021.3085800.

[19] L. S. Xavier, A. F. Cupertino, H. A. Pereira, "Ancillary services provided by photovoltaic inverters: Single and three phase control strategies", *Comput Electric Eng*, vol. 70, pp. 102 – 121, 2018, doi:10.1016/j.compeleceng.2018.03.010.

[20] J. M. S. Callegari, A. L. P. d. Oliveira, L. S. Xavier, A. F. Cupertino, D. I. Brandao, H. A. Pereira, "Voltage Detection-Based Selective Harmonic Current Compensation Strategies for Photovoltaic Inverters", *IEEE Trans Energy Conv*, pp. 1–11, 2023, doi:10.1109/TEC.2023.3238404.

[21] P. Mattavelli, S. Buso, *Digital control in Power Elecronics*, Morgan & Claypool, 2015.

[22] L. S. Araujo, D. I. Brandao, "Self-adaptive control for grid-forming converter with smooth transition between microgrid operating modes", *Int J Elect Power Energy Syst*, vol. 135, p. 107479, 2022, doi:10.1016/j.ijepes.2021.107479.

[23] T. Caldognetto, S. Buso, P. Tenti, D. I. Brandao, "Power-Based Control of Low-Voltage Microgrids", *IEEE J Emerg Sel Topics Power Electron*, vol. 3, no. 4, pp. 1056–1066, 2015, doi:10.1109/JESTPE.2015.2413361.

[24] M. S. Padua, S. M. Deckmann, F. P. Marafao, "Frequency-Adjustable Positive Sequence Detector for Power Conditioning Applications", *in IEEE 36th PESC*, pp. 1928–1934, 2005, doi:10.1109/PESC.2005.1581895.

[25] S. Golestan, M. Ramezani, J. M. Guerrero, F. D. Freijedo, M. Monfared, "Moving Average Filter Based Phase-Locked Loops: Performance Analysis and Design Guidelines", *IEEE Trans Power Electron*, vol. 29, no. 6, pp. 2750–2763, 2014, doi:10.1109/TPEL.2013.2273461.

[26] J. M. S. Callegari, W. F. de Souza, D. I. Brandao, T. R. Oliveira, B. J. Cardoso Filho, "The UFMG Microgrid Laboratory: a Testbed for Advanced Microgrids", *Eletrônica de Potência*, vol. 28, no. 2, p. 163–173, Jun. 2023, doi:10.18618/REP.2023.2.0043, URL: https://journal.sobraep.org.br/index.php/rep/article/view/17.

[27] J. M. S. Callegari, D. I. Brandao, L. G. M. Oliveira, S. M. Silva, B. J. Cardoso Filho, "Advanced Microgrid: Containerized Development Platform", *Eletrônica de Potência*, vol. 30, p. e202502, Jan. 2025, doi:10.18618/REP.e202502, URL: https://journal.sobraep.org.br/index.php/rep/article/view/984.

BIOGRAPHIES

João Marcus Soares Callegari received the B.Sc. degree in electrical engineering from the Federal University of Viçosa, Brazil, in 2019, the M.Sc. degree in electrical engineering from the Federal Center of Technological Education of Minas Gerais, Brazil, in 2021, and the doctorate degree in electrical engineering at the Federal University of Minas Gerais, Brazil, in 2024. His current research and technical interests include the design and control of grid-connected multifunctional inverters, the reliability of power electronics-based systems, and AC microgrids. Mr. Callegari was the recipient of the President Bernardes Silver Medal in 2019 and the IEEE IAS CMD Student Thesis Contest 2022 (Non-PhD Category).

Lucas Savoi Araujo received the Ph.D. degree in electrical engineering from the Federal University of Minas Gerais (UFMG), Belo Horizonte, Brazil, in 2022. He was a Visiting Researcher at University of Padova, Italy, in 2022. His research is related to control of grid-forming converters, control of microgrids, electric transport and power electronics applied to renewable sources and storage systems.

Dener A. de L. Brandão , born in 1994 in Belo Horizonte, Brazil, is an electrical engineer (2018) and holds a master's degree (2021) from the Federal University of Minas Gerais (UFMG). He is currently pursuing a doctorate in Electrical Engineering with a focus on Power Electronics, also at UFMG. Since 2021, he has been a student member of IEEE, and since 2024, a student member of the Brazilian Power Electronics Society (SOBRAEP). His research interests include simultaneous control of microgrids and fast-charging stations, high-power converters for industrial applications, electric drives, power quality, and electric vehicles.

Braz J. Cardoso Filho received the Ph.D. degree in electrical engineering from the University of Wisconsin–Madison, Madison, WI, USA, in 1998. Since 1989, he has been a Faculty Member with the Department of Electrical Engineering, Universidade Federal de Minas Gerais, Belo Horizonte, Brazil, where he is currently a Full Professor, and the Founder and the Head of the TESLA Power Engineering Laboratory. He has authored/co-authored more than 300 technical papers on the topics of power electronics and electrical drives and holds 15 patents and patent applications. His research interests include utility applications of power electronics, renewable energy sources, semiconductor power devices, electrical machines and drives, and vehicle electrification.

Danilo Iglesias Brandão received the doctorate degree in electrical engineering from the State University of Campinas (Unicamp), Brazil, in 2015. He was visiting positions at Colorado School of Mines (2009 and 2013), Università degli Studi di Padova (2014) and Norwegian University of Science and Technology (2018 and 2020). He is currently an assistant professor at Federal University of Minas Gerais (UFMG), Brazil. His main research interests are control of grid-tied converters and microgrids. He is a member of SOBRAEP.